29th Symposium on Naval Hydrodynamics
Gothenburg, Sweden, 26-31 August 2012

Numerical and Experimental Study of Bubble Entrainment due to a Horizontal Plunging Jet

C.-T. Hsiao, X. Wu, J. Ma, and G. L. Chahine
(DYNAFLOW, INC., USA)

ABSTRACT

Free surface disruption, bubble entrainment, and resulting bubbly wake due to a stationary and moving horizontal jets plunging into a quiescent liquid were studied both numerically and experimentally. The moving jet wake showed significantly different flow characteristics than the stationary jet wake. High speed videos revealed that large vortical structures with entrapped air were generated periodically from the horizontal plunging jet. Each vortical air pocket broke up into multiple bubbles due to local shear flows as it returned toward the free surface and moved downstream. The frequency of the air pocket occurrence was analyzed and found to scale with the plunging jet flow and geometry conditions. The plunging dynamics was simulated with an Eulerian/Lagrangian one-way coupled two-phase flow model, which included a Level-Set method and a sub-grid bubble entrainment model. These captured free surface dynamics and predicted the bubble generation and entrainment. The flow structures, velocity field, and overall bubble spreading region near the plunging region were well captured by the numerical model. Further improvement on downstream wake flow is being sought through two-way coupling between the two phases since the one-way coupling does not account properly for the effective density.

INTRODUCTION

Bubble generation and entrainment in the transom region of a surface ship, along its hull, and in breaking following waves are major contributors to the ship signature. For advanced ships, such as the Littoral Combat Ships (LCS) and the Joint High Speed Vessels (JHSV), waterjet propulsion adds another source of air entrainment through the waterjet and free surface interactions in the transom region and beyond. In littoral warfare, such bubbly wakes provide a means to homing torpedoes enabling them to find their target because of the large acoustic cross section of bubbles. While there have been significant research advances to understand bubble generation in breaking waves along conventional ship hull (Melville et al. 1993, Dong et al. 1997, Duncan 2001, Muscari and Mascio 2004), less is known about the impact of waterjet propulsion on the bubbly wake especially when the waterjets are operated above the free surface.

As the liquid jet plunges in the water pool significant air is entrained and forms air pockets. These eventually break up into small bubbles, which travel downstream to contribute to the bubbly wake. Gravity acts as a natural bubble size filter making all large bubble go back to the surface close to the ship, and only very fine bubbles propagate in the wake far downstream. Although many experimental studies (e.g. Sene 1988, Ervine *et al.* 1980, McKeogh and Ervine 1981, Bin 1993, Chanson 1996, Kenneth *et al.* 2011) have been devoted to air entrainment and bubbly flow underneath a plunging jet, most of them have focused on vertical plunging jets. For the current waterjet propulsion application, the jet flow comes out of the nozzle orifice almost horizontally and plunges onto the free surface at a very small angle.

To better understand the underlying flow physics involved in the bubble entrainment process and provide validation data for developing a reliable numerical model, we have conducted an experimental study on horizontal water jet plunging into both quiescent water and in the presence of a relative velocity between the plunging jet and the water. The tests were conducted in two DYNAFLOW tanks: a 5 ft x 5 ft x 72 ft tank and a smaller 2 ft x 2 ft x 80 ft tank equipped with a moving carriage. Various measurement techniques were used to characterize the

jet wake and the flow, including high speed video visualizations and flow velocity measurements with PTV (Particle Tracking Velocimetry), Pitot tubes, and Kiel probes for flow velocity measurements when the bubble density was too high to apply the PTV technique.

In addition to the experimental study, we have developed a two-phase flow model to simulate bubble entrainment due to the jet interacting with the free surface and entraining air. To do so we needed to overcome two major numerical difficulties:

1. The first challenge laid in the jet free surface impact, violent free surface deformation, and the subsequent breakup and mixing in the plunging area. Conventional interface tracking approaches using moving grids to track liquid/gas interfaces were not appropriate for this application because of numerical difficulties with interface folding and break up. Approaches that avoid using moving grids to track the liquid-gas interface deformations have been developed mainly in two categories: Volume of Fluid (VOF) methods (Hirt 1981, Lafaurie *et al.* 1994, Kunz *et al.* 2000, Deshpande et al, 2012) and Level-Set (LS) method (Dabiri et al. 2007, Sussman et al. 1994, Sussman et al. 1998). While both interface capturing methods solve a Navier-Stokes equation with a fixed computational grid using an Eulerian approach, the liquid/gas interface is captured in a very different way. In the VOF method an advection equation for vapor volume fraction is solved and the density is computed according to the volume fraction of the two phases. This method does not have a sharp interface for imposing the boundary condition. In the LS method, the interface location is determined by solving an advection equation for the level-set function, in which the interface is represented as the iso-surface of the level zero. This method provides a sharp interface which allows imposing a boundary condition similar to the interface tracking scheme, i.e. balance of normal stresses and zero shear stress condition. For studying the current plunging jet problem, we have developed an Eulerian two-phase flow model by implementing the LS method in our Navier-Stokes solver, 3DYNAFS-VIS©.

2. The second numerical challenge was to resolve the interface breakup process from entrained large air pockets into micron-sized bubbles. To resolve the transition into small bubbles, a fine spatial resolution of the domain with respect to bubble sizes would be required. However, resolving very small bubbles involves characteristic lengths several orders of magnitude smaller than the grid resolution affordable to the best available computational resources. Instead of refining the mesh to the limit of resolving the small bubbles we have applied a subgrid bubble entrainment model, which releases bubbles into the liquid based on the flow conditions on the liquid/gas interface. Previous studies using a Two-Fluid model (Moraga et al. 2008, Ma *et al.* 2010, Ma *et al.* 2011, Drew and Passman 1998, Lahey 2009) proposed and implemented successfully a subgrid air entrainment model to predict bubble entrainment without fully resolving the breakup process. This model allows bubble release into the liquid from predicted interface locations with a pre-set bubble size distribution. The subgrid air entrainment model was able to quantitatively predict the rate of air entrainment and subsequent dispersion of a bubbly flow for a vertical plunging jet.

The current study aims at resolving better the dynamics of the bubbles based on the Eulerian/Lagrangian coupled approach we have been developing (Hsiao *et al.* 2003, Hsiao and Chahine 2005, Hsiao *et al.* 2006). In this model the plunging jet flow field and the breakup of the entrained air pockets are simulated with an Eulerian continuum-based two-phase flow model, while a Lagrangian discrete bubble model is used to track the small bubbles generated by the subgrid model in the liquid flow. The present study further improves the subgrid air entrainment model by incorporating a bubble breakup model (Martinez-Bazan *et al.* 1999) which allows the initially released bubbles from the predicted interface locations to continue to break up and transition to smaller sizes according to local turbulent shear flow conditions without using a pre-described bubble size distribution.

In the studies described below, simulations of the plunging jet flow field using the Eulerian two-phase flow model is first validated with experimental measurements and then the Eulerian/Lagrangian coupled model with the bubble entrainment model is applied to predict the bubble size distribution in the wake.

EXPERIMENTAL STUDY

Two sets of plunging jet experiments were conducted. The first set considered the interaction of a stationary plunging jet with a quiescent free surface while the second set studied a moving plunging jet relative to the quiescent pool of water.

Experiment Setup

Stationary Plunging Jet Setup

Experiments on the interaction between a stationary plunging jet and a free surface were performed at DYNAFLOW in the 75x5x5 ft^3 wind-wave tank sketched in Figure 1. Most of the side walls of the tank are made of transparent Plexiglas which allows

for visualization of the waterjets, their interaction with the free surface, and bubble entrainment. Height-adjustable supporting rigs were used to mount the nozzle at desired height from the initial water surface level. The flow loop was powered by two 15 hp Goulds pump (Model 3656), capable of 550 gpm at 25 psi. These pumps were connected to the tank with 4 in. (10.16 cm) diameter pipes. Flow rates and pressures were measured by gauges located in line. The flow rate of the nozzle was controlled by a pressure valve, which imposed the upstream pressure. A flow straightener section was used to minimize upstream disturbances reaching the nozzle inlet.

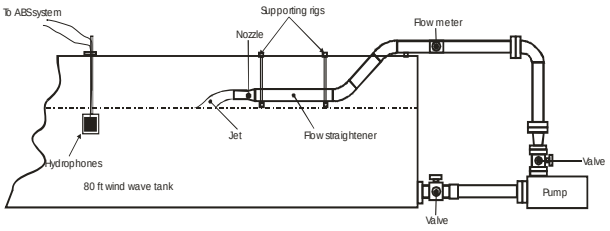

Figure 1: Setup of the experiment for horizontal plunging jet in quiescent water in DYNAFLOW's 75x5x5 ft^3 wind-wave tank.

The nozzle selected for the study had the shape shown in Figure 2, designed to converge smoothly from the 10.16 cm (4 in) PVC pipe to the desired nozzle orifice diameter of 4 cm (1.57 in). A straight section of 10 ft led to the orifice following two 135° bends and a flexible pipe length in between the bends of 10 ft. The flexible hose was used to adjust the nozzle submergence to various depths without needing to empty or add water into the tank. It brought the nozzle down to the required depth. The water jet could thus be easily submerged or placed above the free surface.

Figure 3 shows an overall picture of the jet impacting the free surface and the bubbly wake. Unfortunately, the dark vertical strips are structural beams of the tank which blocked the view at some locations. In the picture, the jet plunges into the free surface at the left edge of the picture.

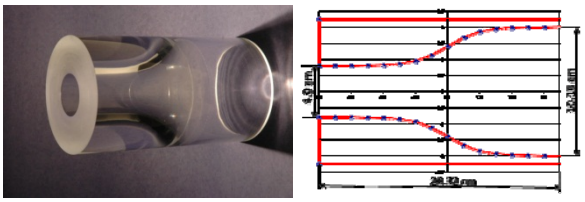

Figure 2: Picture of the Plexiglas nozzle (left) and drawing of its profile (right) with an inlet diameter of 10.16 cm and an orifice diameter of 4 cm.

Figure 3: Overall picture of the plunging jet and its bubbly wake. The jet plunges into the free surface at the left edge of the picture.

Moving Plunging Jet Setup

To investigate the effect of a moving plunging jet, an experiment setup was designed to use our 80 ft long carriage tank, which has a square cross section of 2 ft by 2ft. Figure 4 shows a side-view sketch of the experimental setup. A variable speed reversible electric motor driving system (Graham Drive) was used to drive at the desired speed two carts attached to the driving system through a steel cable. The first carriage cart operated as the jet generation platform on which sat the jet nozzle, the pump, a water reservoir tank, and appropriate plumbing to generate the plunging jet. The pump drove the water from the reservoir to the nozzle to form the plunging jet. A valve and a flow meter were used to regulate the flow rate and achieve the desired jet exit velocity. The other carriage cart worked as an instrumentation platform, where various data acquisition and instrumentation equipment, such as a high speed camera system, a DAQ system, wave probes, etc., were mounted. The two carriages were interconnected through two 1 in. aluminum framing tubes and the separation distance between the two carts could be adjusted to place instrumentation at the desired downstream location.

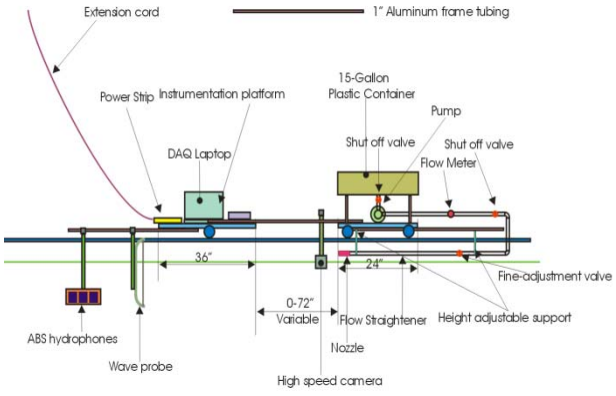

Figure 4: Side-view sketch of the experimental setup for the moving plunging jet experiments.

Figure 5 shows an overall view of the experimental setup, at the front end of the towing tank is the Graham Drive and the interconnected carriage carts can be seen on top of the tank rails.

Figure 5: A picture of the overall carriage tank used for the moving plunging jet experiments.

Velocity Field Measurement

To enable flow field visualizations and measurements a Redlake Motionscope PCI high speed video imaging system capable of 6,000 frames per second with a MiDAS integrated data acquisition system was used. Due to the large bubble density generated, it was difficult to utilize flow velocity measurement techniques such as PIV (Particle imaging Velocimetry) in the region close to the jet impinging area. A PTV (Particle Tacking Velocimetry) technique was developed to take advantage of our high speed video cameras by measuring the velocities obtained by tracking the bubble motions.

The video images were the processed using the following steps:

- The images from a high speed movie were first enhanced using a particle tracking technique to isolate individual particle/bubbles. Figure 6 shows a sample image before image analysis and the same image after processing.
- The processed images were then paired up in sequence for cross correlation processing.
- A cross correlation scheme, similar to that for the PIV analysis, was then used to process the image pairs to obtain the time-dependent spatial velocity flow field.
- The velocity vector map was finally fed to post-processing routines to obtain velocity profiles, etc. at a given location.

Figure 7 shows an example velocity profile measured at 175 cm downstream from the nozzle. With the bubble tracking scheme we can obtain the complete jet wake flow field. This corresponds to a jet exit velocity of 4 m/s with the nozzle axis located one diameter above the free surface.

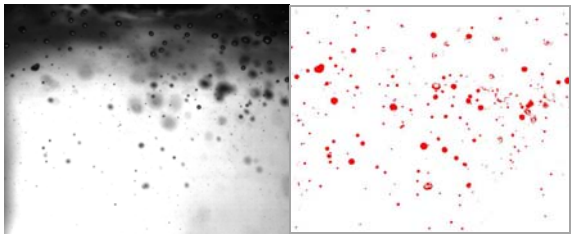

Figure 6: Sample images used for PTV. The original image (left) and the processed image (right).

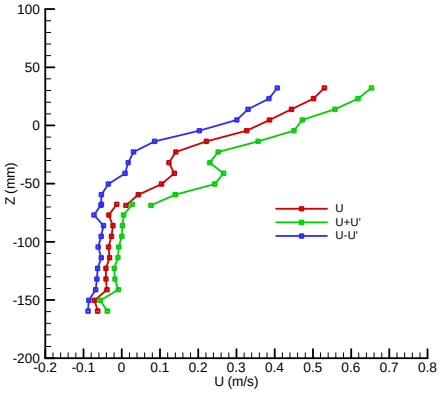

Figure 7: Velocity profiles (mean and fluctuations) at 175 cm downstream from the nozzle based on PTV measurement. Jet exit velocity=4 m/s. Nozzle axis one orifice diameter above free surface.

Figure 8 shows a sample vector map overlaid with one of the images used in the tracking scheme to obtain the velocity measurements. As we can see, except for the dense high void fraction in the middle regions, velocity is measured in both the lower and top region of the jet wake. The velocity in the upper region includes not only the surface wave motion but also motions of water droplets that break from the surface wave.

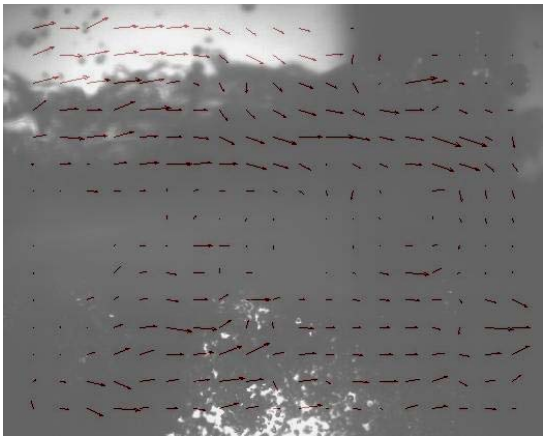

Figure 8: Sample vector map obtained by tracking individual bubble/water droplet motion.

Figure 9 shows a sample instantaneous velocity contour map of the jet wake right downstream of the impingement area. In order to obtain the measurement of the complete flow field, measurements in different overlapping areas were conducted. To provide a time-averaged velocity field for numerical validation, the velocity contours were averaged from all video frames. Figure 10 shows the contour map of the averaged velocity field of the jet wake, where the zero in the vertical z axis is the reference initial position of the free surface. The higher horizontal velocity region corresponds to the droplet formation area. It is thick initially where mixing, droplets, and bubbles develop. It becomes thinner as the jet wake travels downstream and large bubbles rise to the free surface. As the jet wake evolves downstream, the flow velocity decreases.

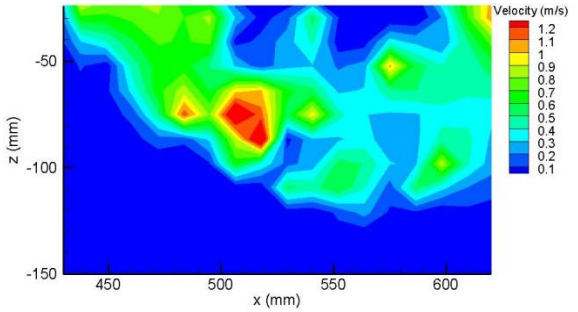

Figure 9: Sample contour map of the velocity flow field below the horizontal plunging jet.

The horizontally blanked out area is the region where the impingement and mixing of the jet occur most intensely and the void fraction is so high that the bubble tracking scheme fails as no individual bubble tracking is possible. As for the vertically blanked out regions, these are the areas where the wave tank frames blocked the optical access. Also noteworthy is the section above z = 0 mm between x = 500 ~ 1,000 mm, where higher average velocities were measured., These are not bubble velocities, but correspond to the contribution from water droplet velocities, as this region is where the surface wave breaks into droplets.

To characterize regions where the bubble density was too high to allow use of the PTV method, Pitot tube measurements were conducted. To interpret the Pitot tube readings in a bubbly medium we used the model of Bosio & Malnes (1969), which corrects for the void fraction, α, as follows:

$$V_L = \frac{1}{\sqrt{(1-\alpha^2/2)}}\sqrt{\frac{2\Delta P}{\rho_L}}, \qquad (1)$$

where ΔP is the pressure difference read by the Pitot tube. This equation showed best prediction capability with errors less than 15% in their studies.

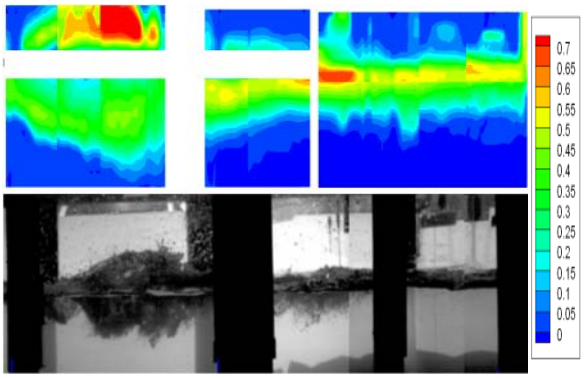

Figure 10: Streamwise velocity contour map of the jet wake.

Since we were not able to measure accurately the local void fraction in the plunging zone, we used an average value of 0.25 to apply Equation (1) and enable the contours to match with the PTV measurements at the edges of the two regions.

Figure 11 shows the combined estimated velocities from both PTV and Pitot tube measurements. It is seen that a complete velocity profile can be obtained through the whole region with the combined techniques.

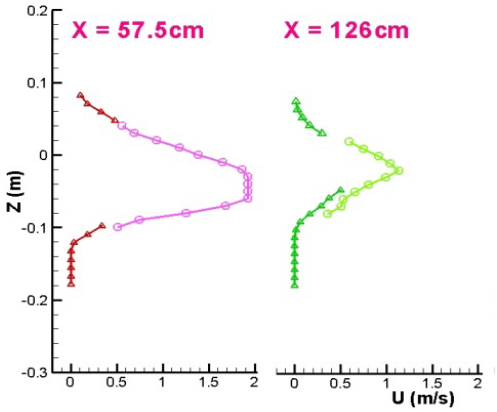

Figure 11: Velocity profiles at two locations downstream of orifice exit using combined PTV and Pitot tube measurements.

Flow Structure Characterization

The results reported below for the moving plunging jet experiments were obtained for a nozzle exit velocity of 4 m/s with the carriage moving at 2 m/s in the opposite direction of the jet flow. The moving jet wake, as expected, showed significantly different flow characteristics than the stationary jet wake.

Figure 12 shows pictures of the moving jet wake (top) and the stationary jet wake (bottom). Both jets were generated from the same 1.68 cm nozzle with

all other conditions the same except for that the nozzle was moving at 2 m/s in the moving jet wake case and was stationary in the stationary jet wake case. The camera was at a fixed position with respect to the nozzle and the field of view for both cases was the same and covered the range of horizontal distance to the nozzle exit from 32 to 64 cm. As shown in the figure, the number of vortical structures below the free surface was much higher in the moving jet wake case than in the stationary jet wake case. The depths of the pockets were also much smaller. These differences can partially be attributed to the slower jet velocity relative to the free surface (2 m/s) in the moving jet wake case compared to the stationary jet wake case (4 m/s).

From the high speed movies it can be seen that as the jet plunges onto the free surface, a large amount of air is entrained to form periodically a large air pocket region with high vorticity. The frequency of formation depends on the jet conditions. Based on the high speed movies, we were able to measure the frequency of the occurrence at different downstream locations. It is evident from the visualizations that flow structures merge as they advance downstream and thus the large structure occurrence frequency decreases with increasing distance from the nozzle.

An image analysis scheme tracked the bottom boundary position of the two-phase structures at a selected location. It used a 10-pixel wide section from the image centered at the selected location and detected the bottom boundary. FFT was then performed on the time variation of this boundary position to obtain a frequency spectrum and the dominant frequency in the spectrum was identified as the frequency of passage.

Figure 14 shows the analysis of the time variations of the boundary positions for both jet wakes. The frequency of the two-phase structure position is much higher and the oscillation amplitude smaller for the moving jet wake, relative to the stationary jet. In both cases, the dominant frequency decreases when moving downstream away from the nozzle.

Analysis of the results of the observations for three different nozzle diameters, D = 1.68 cm, 4 cm, and 8 cm, at the same normalized distance from the nozzle, X/D, are shown in Figure 14. The frequency of the flow structure of the small 1.68 cm nozzle is much higher for the same X/D. The three nozzles could not however be run for the same ratio of standoff distance between nozzle center and free surface divided by the nozzle diameter due to practical hardware constraints. This ratio was 1.81 for the 1.68 cm nozzle while it was 1.0 for the 4 cm and 8 cm nozzles.

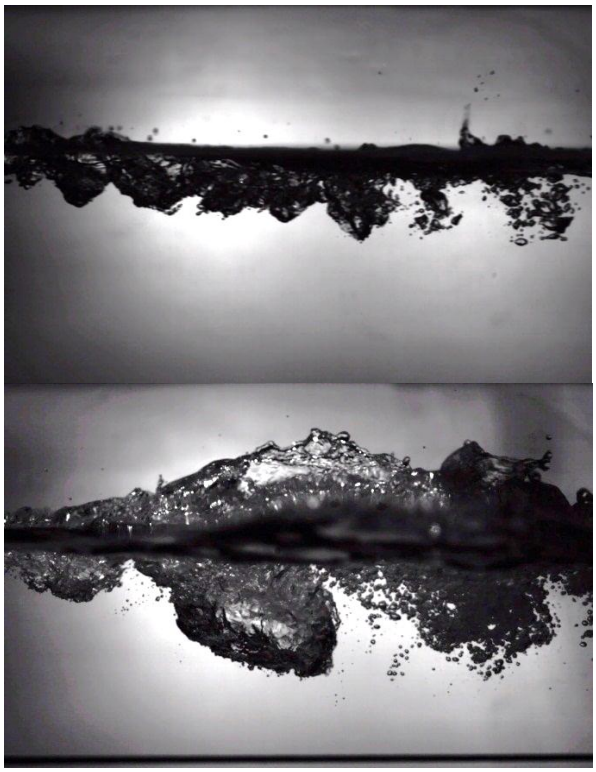

Figure 12: Comparison of the flow structure for the moving plunging jet wake (top) and the stationary plunging jet wake (bottom). Nozzle diameter was 1.68 cm. Field of view: 32cm to 64 cm from the nozzle exit. Relative velocity between jet and nozzle is 4m/s for both cases. The carriage speed and the jet speed were 2m/s for the moving jet.

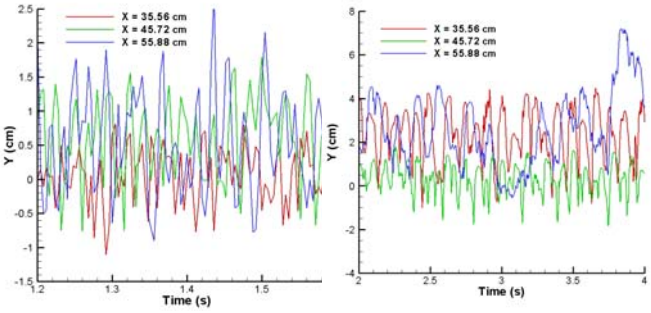

Figure 13: Variation of the positions of bottom boundary of vortices for moving jet wake (left) and stationary jet wake (right).

If we consider that the time needed for the depression made by the plunging jet free surface to return to its initial position is determined by the gravitational restoring force, the restoration time scale would be related with D_{cav} / g, where D_{cav} is the cavity depth and g is the gravitational acceleration. This

would give a normalization for f as $\sqrt{D_{cav}/\mathrm{g}}$. A resulting non-dimensional parameter would be

$$\overline{f}^2 = f^2 \frac{D_{cav}}{g} . \qquad (2)$$

D_{cav} should be related to the nozzle diameter, D, the standoff vertical distance between the jet and the free surface, $D_{s,}$ and the relative velocity between the jet and the free surface, V_{rel}. We found empirically that with

$$\overline{f}^2 = f^2 \frac{D}{g}\left(\frac{D}{D_s}\right)\left(1+k\frac{V_{rel}^2}{Dg}\right)^{-1} , \qquad (3)$$

all conditions practically collapse over each other as shown in Figure 16 if k is set to 20. In Equation (3), k is a constant that relates the jet frequency with the relative velocity between the nozzle and free surface.

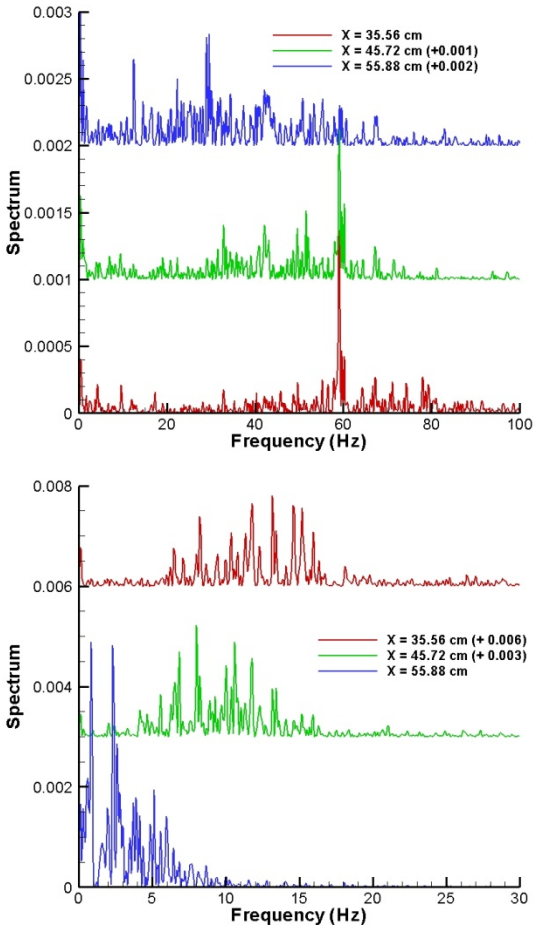

Figure 14: Frequency spectra of the flow structure passage at different downstream locations for both moving (top) and stationary (bottom) jet wakes.

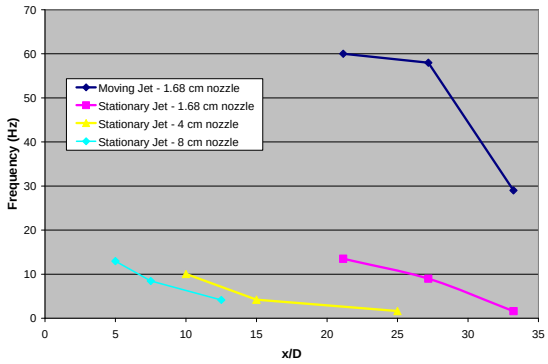

Figure 15: Variation of the dominant frequency of the vortical flow structures with the normalized distance for the moving and stationary jet wakes using different nozzles.

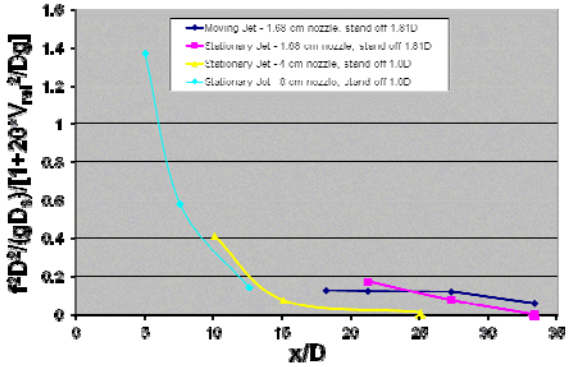

Figure 16: Normalized frequency variation of vortices with normalized distance from nozzle for different nozzles**.**

Bubble Entrainment Visualization

In addition to the flow structure analysis, we used high speed videos to observe how bubbles became entrained to form the bubbly wake. Figure 17 shows close-up views of the jet wake at three different locations downstream of the impact location. It can be seen that the entrained air pocket evolves and breaks up into bubbles while moving downstream

To better understand how the entrained air pocket breaks up to form small bubbles, a high speed movie time sequence of the entrained air pocket near the impinging area is shown in Figure 18. Continual bubble generation can be seen as the cavity retracts from the observed upstream location. A vortical structure is formed and as it moves downstream collapses and breaks up into multiple bubbles and blobs. The large blobs then continue breaking into a bubble clouds as they move downstream and are exposed to the shear. This implies the bubble breakup is highly dependent on the local shear flow.

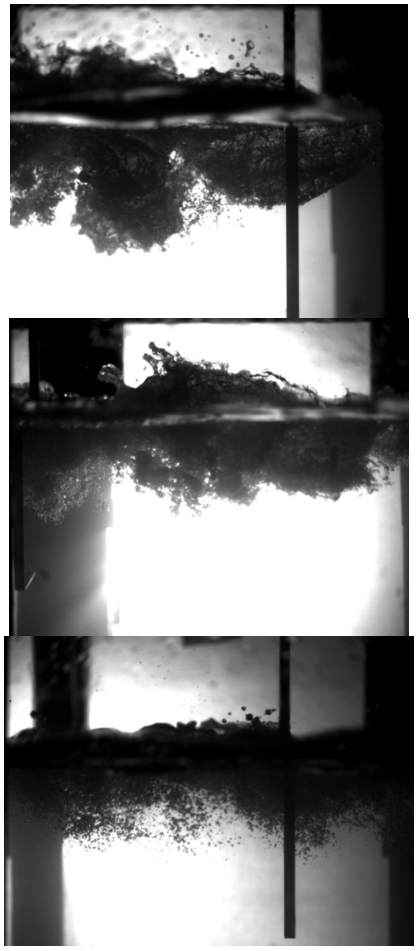

Figure 17: Sample image of close-up view of the jet wake at 50 cm (top) , 100 cm (middle), and 125 cm (bottom) downstream from the nozzle exit.

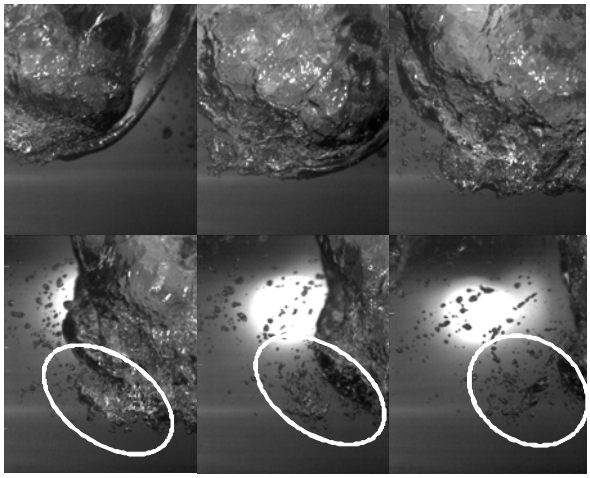

Figure 18: High speed sequence from a high speed movie showing bubble generation from a vortical large structure, which trails the large cavity motion as it recesses toward the free surface.

Bubble size distribution measurement

Both an ABS ACOUSTIC BUBBLE SPECTROMETER© and optical techniques were used to measure the evolution of the bubble size distribution and void fraction with the jet wake development. Figure 19 shows the setup of the ABS system for bubble size distribution and void fraction measurement in the jet wake. A triple-set hydrophone system was used, including a 50 kHz, a 150 kHz, and a 250 kHz hydrophone pairs to achieve maximum measurement range coverage.

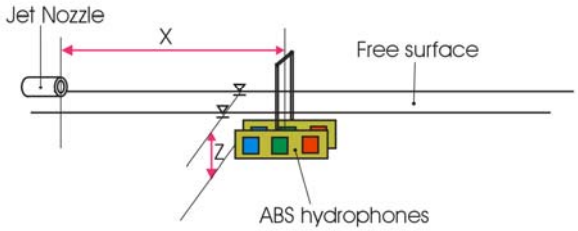

Figure 19: Set up of the ABS for bubble distribution measurements in the jet wake.

Figure 20 shows a sample comparison of bubble size distribution between the ABS measurement and the optical imaging method. As we can see from the figure, the optical imaging method is capable of discriminating large bubbles that are outside the measurement range of the ABS system, while the ABS system is capable of measuring small bubble sizes below 200 microns that are below the resolution of the optical imaging. In the overlapping region, from 200 to 1,000 microns, the results from the two methods are similar.

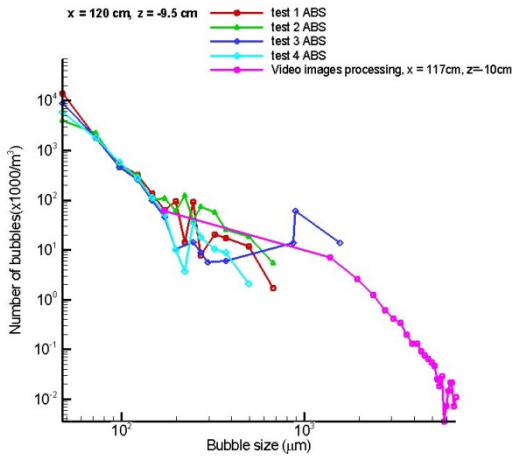

Figure 20: Example comparison of bubble size distributions in the jet wake between the ABS and optical image measurements.

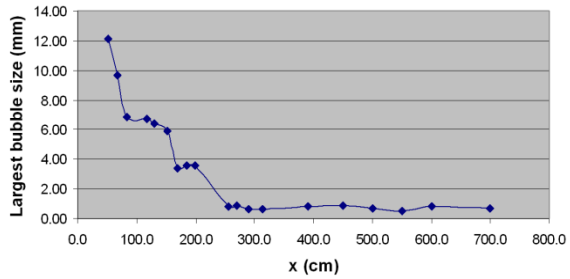

Figure 21: Variation of the largest bubble radius with the downstream distance from the plunging jet impact region.

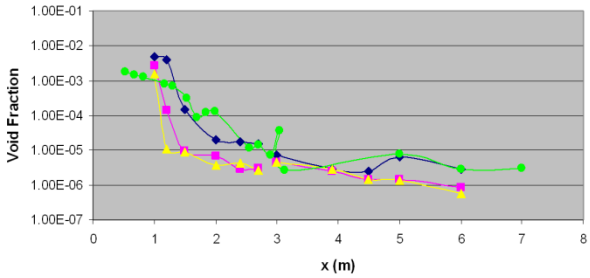

Figure 22: Decrease of the void fraction in the jet wake with the distance downstream from the plunging jet impact location.

Figure 21 shows the variation of largest bubble radius with the distance from the nozzle. Three meters downstream of the nozzle (i.e. 75 jet diameters), the largest bubble sizes have decreased to less than 1 mm. The trend of the decreasing bubble numbers and decreasing bubble sizes with the downstream distance from the nozzle is also reflected in Figure 22, which shows repeated void fraction measurements, which shows strong void fraction decrease from 10^{-3} at x = 1 m to the 10^{-5} range after x = 3 m, as large bubbles break up or rise to the free surface as the distance downstream from the nozzle increases.

NUMERICAL STUDY

To numerically study the bubble entrainment due to the plunging jet interacting with free surface, we have employed an Eulerian/Lagrangian coupled two-phase flow model. The Eulerian model addresses the continuum-based two-phase model and is coupled with a discrete bubble model tracking bubble motion using a Lagrangian approach.

Eulerian Continuum-Based Two-Phase Model

The Eulerian continuum-based two-phase model uses DYNAFLOW's Navier-Stokes solver, 3DYNAFS-VIS© , which includes a Level-Set method for simulation of large-deformation free surface flows.

Navier-Stokes Solver

3DYNAFS-VIS© solves three-dimensional unsteady incompressible continuity and momentum equations:

$$\frac{\partial u_i}{\partial x_i} = 0 \,, \tag{4}$$

$$\frac{\partial u_i}{\partial t} + u_j \frac{\partial u_i}{\partial x_j} = -\frac{\partial p}{\partial x_i} + \frac{1}{R_e}\frac{\partial \tau_{ij}}{\partial x_j} \,, \tag{5}$$

where $u_i = (u, v, w)$ are the Cartesian components of the velocity, $x_i = (x, y, z)$ are the Cartesian coordinates, and p is the pressure. The effective stress tensor τ_{ij} is given by:

$$\tau_{ij} = \left[\left(\frac{\partial u_i}{\partial x_j} + \frac{\partial u_j}{\partial x_i} \right) - \frac{2}{3}\delta_{ij}\frac{\partial u_k}{\partial x_k} \right] , \tag{6}$$

where $R_e = \rho u^* L^* / \mu$ is the Reynolds number, u^* and L^* are the characteristic velocity and length, ρ is the liquid density, μ is its dynamic viscosity, and δ_{ij} is the Kronecker delta.

The solver is based on the artificial-compressibility method (Chorin 1967) in which a time derivative of the pressure multiplied by an artificial-compressibility factor, β, is added to the continuity equation as

$$\frac{1}{\beta}\frac{\partial p}{\partial \tau} + \nabla \cdot \mathbf{u} = 0 \,. \tag{7}$$

As a consequence, a hyperbolic system of equations is formed and can be solved using a time marching scheme. This method can be marched in pseudo-time to reach a steady-state solution. To obtain a time-dependent solution, a Newton iterative procedure is performed at each physical time step in order to satisfy the continuity equation.

3DYNAFS-VIS© uses a finite volume formulation. First-order Euler implicit differencing is applied to the time derivatives. The spatial differencing of the convective terms uses the flux-difference splitting scheme based on Roe's method (Roe 1981) and van Leer's MUSCL method (Van Leer 1979) for obtaining the first-order and the third-order fluxes, respectively. A second-order central differencing is used for the viscous terms which are simplified using the thin-layer approximation. The flux Jacobians required in an implicit scheme are obtained numerically. The resulting system of algebraic equations is solved using the Discretized Newton Relaxation method (Vanden, and Whitfield 1995) in which symmetric block Gauss-Seidel sub-

iterations are performed before the solution is updated at each Newton iteration.

Level-Set Method

In order to enable 3DYNAFS-VIS© to simulate the large free surface deformations such as folding and breakup in the plunging jet problem, we have implemented a two-phase model based on the Level-Set method. To do so, a smooth function $\varphi(x,y,z,t)$, whose zero level coincides at $t = 0$ with the liquid/gas interface, is defined in the whole physical domain (i.e. in both liquid and gas phases) as the signed distance $d(x,y,z)$ from the interface:

$$\varphi(x,y,z,0) = d(x,y,z). \tag{8}$$

This function is enforced to be a material surface at each time step using:

$$\frac{d\varphi}{dt} = \frac{\partial\varphi}{\partial t} + u_j \frac{\partial\varphi}{\partial x_j} = 0, \tag{9}$$

where u is the velocity of interface. However, the integration of Equation (9) does not ensure that the thickness of the jump region remains constant in space and time during the computations because the value of φ may get diffused by numerical viscosity and distorted by the flow field. To avoid this problem (noting that if φ is the correct distance, then $|\nabla\varphi| = 1$) a new distance function is constructed by solving a "re-initialization equation" in pseudo time iterations (Sussman 1998):

$$\frac{\partial\varphi}{\partial\tau} = S(\varphi_0)\left[1 - |\nabla\varphi|\right], \tag{10}$$

where τ is the pseudo time, φ_0 is the initial distribution of φ, and $S(\varphi_0)$ is a sign function, which is zero at the interface.

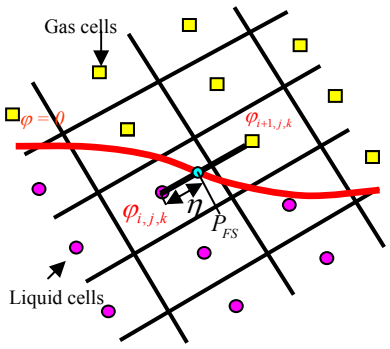

Figure 23: Cell location identification in the computational domain.

In a standard Level-Set approach both liquid and gas phases of the fluid are solved separately using Equations (4) and (5) after identifying to which phase a concerned cell belongs and applying a smoothed Heaviside function over a thickness of the interface to smooth the fluid properties. Figure 23 illustrates the identification of the cells according to the zero level-set.

Instead of solving both phases, we have implemented a single phase level-set method using the Ghost Fluid Method (Fedkiw *et al.* 1999, Kang *et al.* 2000) to maintain a sharper interface. This method allows imposing the dynamics boundary conditions across the interface without use of smoothing functions. If the shear due to the air is neglected, the dynamic boundary conditions (balance of normal stresses and zero shear) can be written:

$$p = \tau_{ij} n_i n_j + \frac{gz}{\rho} + \frac{\gamma\kappa}{\rho}, \quad \tau_{ij} n_i t_j^1 = 0, \quad \tau_{ij} n_i t_j^2 = 0,$$
$$\tau_{ij} = \frac{\mu}{\rho}\left(\frac{\partial u_i}{\partial x_j} + \frac{\partial u_j}{\partial x_i}\right), \tag{11}$$

where g is the acceleration of gravity, γ is the surface tension, μ is the kinematic viscosity and $\kappa = \nabla\cdot\nabla\varphi/|\nabla\varphi|$ is the surface curvature. $\vec{n}$, $\vec{t}^1$, and $\vec{t}^2$ are the surface normal and two tangential unit vectors, respectively. In this approach one or more ghost cells are used to impose the boundary conditions when the interface cells are solved. The interface cells for each phase are identified when one of the following six inequalities is satisfied for two adjacent cells:

$$\varphi_{i,j,k}\varphi_{i\pm1,j,k} < 0,$$
$$\varphi_{i,j,k}\varphi_{i,j\pm1,k} < 0, \tag{12}$$
$$\varphi_{i,j,k}\varphi_{i,j,k\pm1} < 0.$$

Although the Ghost Fluid Method can reduce the grid resolution near the interface and maintain a sharp interface, additional computational cost is still required for the cells in the ignored phase, e.g. air. To further reduce the computational cost for such problems we have applied a single-phase level-set approach in which only the liquid phase of the fluid is solved, while the cells belonging to the gas phase are deactivated during the computations. To solve Equation (9) we use the velocity information from the gas cells which are near the interface. To obtain this information, we assume the following condition across the interface:

$$\mathbf{n}\cdot\nabla u_i = 0, \quad \mathbf{n} = \nabla\varphi/|\nabla\varphi|, \tag{13}$$

which means there is no normal component of the velocity gradient at the interface, while shear could exist. With this assumption we can extend the velocity from the liquid phase along the normal

direction of the distance function to the gas phase by solving the pseudo time iteration equation:

$$\frac{\partial u_i}{\partial \tau} + \mathbf{n} \cdot \nabla u_i = 0. \tag{14}$$

Lagrangian Discrete Bubble Model

The Lagrangian discrete bubble model is based on DYNAFLOW's discrete singularity model, 3DYNAFS-DSM©, which uses a Surface Average Pressure (SAP) approach (Hsiao *et al.* 2003, Choi *et al.* 2004) to average fluid quantities along the bubble surface. This model has been shown to produce accurate results when compared to full 3D two-way interaction computations (Hsiao and Chahine 2003) The averaging scheme allows one to consider only a spherical equivalent bubble and use a modified Rayleigh-Plesset equation (Hsiao *et al.* 2003) to describe the bubble dynamics,

$$R\ddot{R} + \frac{3}{2}\dot{R}^2 = \frac{1}{\rho}\left(p_v + p_{g0}\left(\frac{R_0}{R}\right)^{3\lambda} - P_{enc} - \frac{2\gamma}{R} - \frac{4\mu\dot{R}}{R} \right) + \frac{|\mathbf{u}_s|^2}{4}, \tag{15}$$

where $\mathbf{u}_s = \mathbf{u}_{enc} - \mathbf{u}_b$, R and R_0 are the bubble radii and time t and 0, p_v is the liquid vapor pressure, p_{g0} is the initial bubble gas pressure, λ is the polytropic compression constant, $\mathbf{u}_b$ is the bubble travel velocity, while $\mathbf{u}_{enc}$ and P_{enc} are respectively the liquid velocity and the ambient pressure "seen" by the bubble during its travel. With the SAP model, $\mathbf{u}_{enc}$ and P_{enc} are respectively the averages of the liquid velocities and pressures over the bubble surface.

A bubble trajectory is obtained from the following bubble motion equation:

$$\frac{d\mathbf{u}_b}{dt} = \left(\frac{\rho}{\rho_b}\right)\left[\frac{3}{8R} C_D |\mathbf{u}_s| \mathbf{u}_s + \frac{1}{2}\left(\frac{d\mathbf{u}_{enc}}{dt} - \frac{d\mathbf{u}_b}{dt} \right) + \frac{3\dot{R}}{2R}\mathbf{u}_s - \frac{\nabla p}{\rho} + \frac{(\rho_b - \rho)}{\rho} g + \frac{3C_L}{4\pi}\frac{\sqrt{\nu}}{R}\frac{\mathbf{u}_s \times \boldsymbol{\Omega}}{\sqrt{|\boldsymbol{\Omega}|}} \right], \tag{16}$$

where ρ_b is the air density, C_D is the drag coefficient given by an empirical equation from Haberman and Morton (1953), C_L is the lift coefficient and Ω is the deformation tensor. The 1st right hand side term is a drag force. The 2nd and 3rd terms account for the added mass. The 4th term accounts for the presence of a pressure gradient, while the 5th term accounts for gravity and 6th term is a lift force (Saffman 1965).

Subgrid Bubble Entrainment Model

To simulate the bubble entrainment process due to air pocket breakup, which is not directly resolved, we have implemented into the code a sub-grid bubble release scheme which can emit bubbles into the water from the air/liquid interface based on the physics and free surface turbulence. This model has recently been validated and successfully used to quantitatively predict air entrainment rates and bubble concentrations beneath plunging jets, in hydraulic jumps and around naval surface ship hulls (Ma *et al*. 2011). The model assumes that the turbulence in the liquid produces a rough air/liquid interface with cavities of a certain size. These cavities may be entrained into the liquid once the downward liquid velocity exceeds the downward velocity of the interface. This leads to a simple expression for the location and rate of air entrainment that is proportional to the liquid's local turbulent kinetic energy times the gradient of the liquid velocity in the downward (i.e., pointed away from the interface and into the liquid) direction.

Specifically, this model follows the following form for the volume of air entrained, q, per unit interface area and unit time:

$$q(\mathbf{x}) = \frac{C_{ent}}{g} k(\mathbf{x}) \frac{\partial u_n}{\partial n}(\mathbf{x}), \tag{17}$$

where $\mathbf{x}$ is the location vector, C_{ent} is a model coefficient, k is the local turbulent kinetic energy of the liquid, and $\partial u_n/\partial n$ is the normal derivative of the normal component of the liquid velocity at the interface. Since no turbulence model is applied in the current simulation, the turbulent kinetic energy is deduced from the fluctuation velocities, $\mathbf{u}'$, obtained by subtracting the time-averaged solution from the instantaneous unsteady solution.

This model gives the entrained air flux as a volumetric flow rate per unit interfacial area. Based on the fact that bubbles can only be entrained into the liquid through a thin layer near the free surface, we can further convert this into a volumetric source by distributing the bubbles into a layer that is φ_{ent} thick below the free surface. So the rate of air entrainment per unit volume, per unit time, is

$$Q(x) = \frac{q(x)}{\varphi_{ent}} = \frac{C_{ent}}{g\varphi_{ent}} k(x) \frac{\partial u_n}{\partial n}(x). \tag{18}$$

This determines the volume of entrained air in a gird cell during a time step or for certain time duration

$$V_b = Q V_{cell} \Delta t, \tag{19}$$

where Δt the time interval during which the bubbles are released.

This volume of entrained air in each active cell is first treated as a single bubble of size $D_o = \sqrt[3]{6V_b/\pi}$. After that, the bubble breakup model of Martinez-Bazan *et al.* (1999) is used to further break up the bubbles into smaller ones according to local flow conditions. Three factors of the breakup process are modeled: a) the breakup frequency, $g(D)$; b) the average number of daughter bubbles formed from the breakup of the mother bubble with a size of D_o, $m(D_o)$; and c) the probability density function (PDF) of the daughter bubbles $f(D;D_o)$. Martinez-Bazan et al. (1999) modeled these three by the following equations:

$$g(\varepsilon, D_o) = K_g \frac{\sqrt{8.2(\varepsilon D_o)^{2/3} - 12\gamma/(\rho D_o)}}{D_o}, \quad (20)$$

$$m(D_o) = 2, \quad (21)$$

$$f(D;D_o) = \frac{1}{D_o} \frac{\left[D^{*2/3} - \Lambda^{5/3}\right]\left[\left(1-D^{*3}\right)^{2/9} - \Lambda^{5/3}\right]}{\int_0^1 \left[D^{*2/3} - \Lambda^{5/3}\right]\left[\left(1-D^{*3}\right)^{2/9} - \Lambda^{5/3}\right] dD^*}, \quad (22)$$

where $D^*=D/D_0$, ε is the turbulent dissipation rate deduced from the fluctuating and mean velocity fields similarly as turbulence kinetic energy described above, K_g is a constant found experimentally to be equal to 0.25, and

$$\Lambda = D_c/D_o, \quad \text{and} \quad D_c = \left(12\sigma/(\beta\rho)\right)^{3/5} \varepsilon^{-2/5}, \quad (23)$$

where D_c is a critical diameter defined as the diameter where the average deformation energy to break up the bubble equals the confinement energy of the bubble. The constant β = 8.2 was obtained from turbulence theory. The number of daughter bubbles, $m(D_o)$, was assumed to be 2, i.e., a binary splitting. Martinez-Bazan *et al.* (1999) showed that the above model predicts very well experimental observations made with air bubbles from a needle injector to a surrounding annulus turbulent water jet.

Numerical Setup

To simulate the plunging jet problem we used a structured grid containing 13.7 million grid points for a computational domain which starts from where the water leaves the jet orifice and ends at 3 meters downstream. The width of the side walls from the center plane and the depth of the bottom from the free surface were 0.36 m and 0.72 m, respectively. The top boundary was located at 0. 2 m above the free surface. Figure 24a shows the grid of the full computational domain used for the simulations. The grid was distributed such that the high grid concentration was near the plunging area and near the center plane with a minimum grid spacing of $\Delta x \times \Delta y \times \Delta z$ = $0.35 \times 0.14 \times 0.15$ cm^3 (see Figure 24c).

In the same picture, the boundary conditions are also displayed. A no-slip condition was applied at the side and bottom walls and at the inlet plane except at the location of jet orifice where a uniform velocity of 4m/s was specified in a circular area with a diameter of 0.04m. A zero gradient condition was specified at the outlet boundary. No particular boundary conditions were required at the top boundary as long as the liquid does not reach the top boundary because the single-phase level set method does not solve the cells in the air region. The jet orifice center was located at an elevation of one diameter above the water free surface.

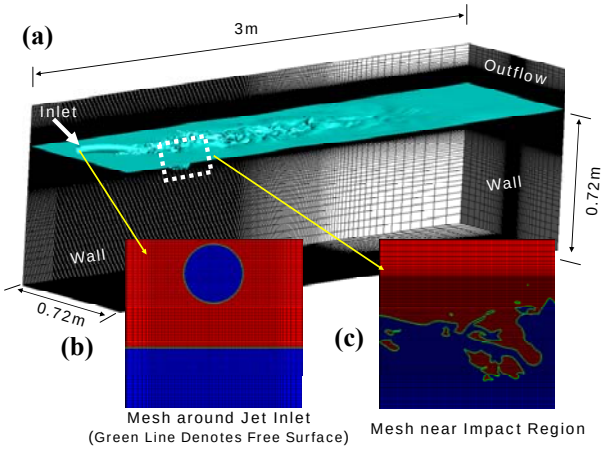

Figure 24: The computational domain, and grid and boundary conditions used for the plunging jet computation: (a) overall view, (b) around the jet inlet, (c) near the plunging area.

Unsteady Simulations of Horizontal Plunging Jets

The simulation started at time = 0 when the jet exited the orifice. The water in the tank was initially quiescent. The simulation was conducted without applying any turbulence model. Figure 25 and Figure 26 show the evolution of the distance function iso-surface of φ = 0 (i.e. liquid/air interface) over a period of one second. This iso-surface illustrates entrained air pockets and bubbles under the waterline while showing liquid splash and droplets above the water line. This representation of the jet and the free surface interaction shows the initial jet plunging phenomenon. It is seen that an initial large air pocket is entrained into the liquid and soon breaks up into small air pockets as it travels downstream. From there on, there appears to be a quasi-periodic behavior with

the free surface tending to "fold", as in a breaking wave, periodically onto the plunging jet in the region of interaction.

It is well-known that the smallest scale of the flow structure at the liquid/air interface which can be resolved is highly dependent on the grid resolution. To study the effect of grid resolution on the simulation, we conducted simulations with three grid resolutions: coarse (1.53×10^6), medium (4.34×10^6), and fine (13.7×10^6) which correspond to a minimum grid spacing of $0.8\times0.52\times0.4$ cm^3, $0.48\times0.26\times0.24$ cm^3, and $0.35\times0.14\times0.15$ cm^3, respectively. Figure 27 shows the three grid resolutions near the plunging area with the first air pocket generated due to this impact in the background to give a sense of the effect of grid resolution with pocket size. It is found that all three meshes captured very similar structure of the big pocket created due the first impinging of jet into the water pool, in terms of pocket size, orientation, and penetration depth. As this pocket starts to break up due to the shearing of the strong velocity gradient near the impact region, the difference between the three meshes becomes more pronounced.

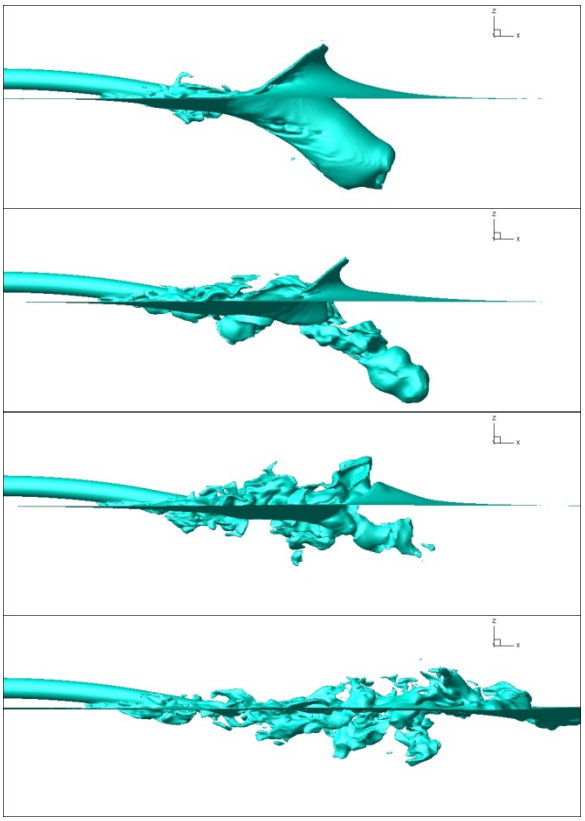

Figure 25: Time sequence of liquid/gas interface deformations as a water jet plunges into a quiescent free surface. Figures illustrated by liquid/air interface iso-surfaces $\varphi = 0$.

Figure 28 compares the results for these three grids at a much later time when the plunging jet wake has fully developed. It is seen that for the case of coarse mesh, the pocket completely separated from the free surface and traveled deep into the water, but necking structure partially connecting the pocket and free surface was observed in the fine mesh. This indicates the fine mesh captured the transition process of air pocket breakup while the coarse mesh did not.

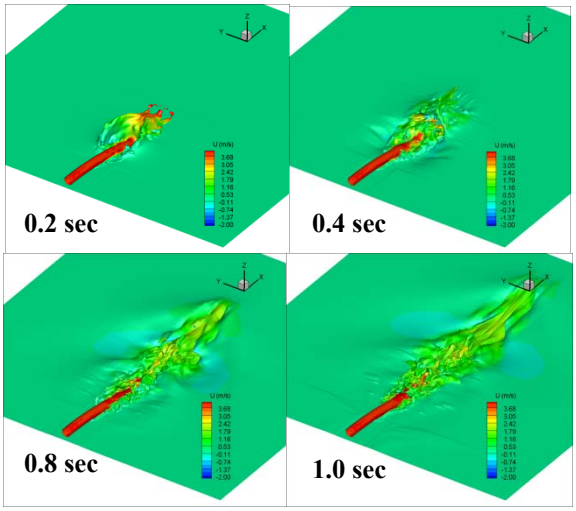

Figure 26: Perspective view of the distance function iso-surface $\varphi = 0$, representing the interface between air and water, colored with streamwise velocity at different time instances.

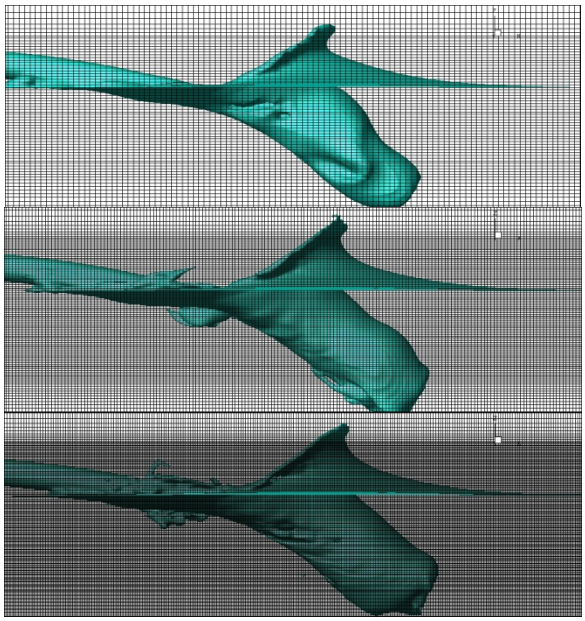

Figure 27: Grids used for the grid dependence calculations with minimum grid spacing of $\Delta x\times\Delta y\times\Delta z$ $=0.8\times0.52\times0.4$cm^3 (top),$0.48\times0.26\times0.24$cm^3 (middle), and $0.35\times0.14\times0.15$cm^3 (bottom), respectively.

This trend further becomes clear after the flow was fully developed as can be seen in the results at time sequence of 4.2s. It can be seen that very fine structures (both droplets above the free surface and air bubbles beneath it) in the fine mesh case while these structures were totally absent in the coarse mesh case and the medium mesh case captured part of them.

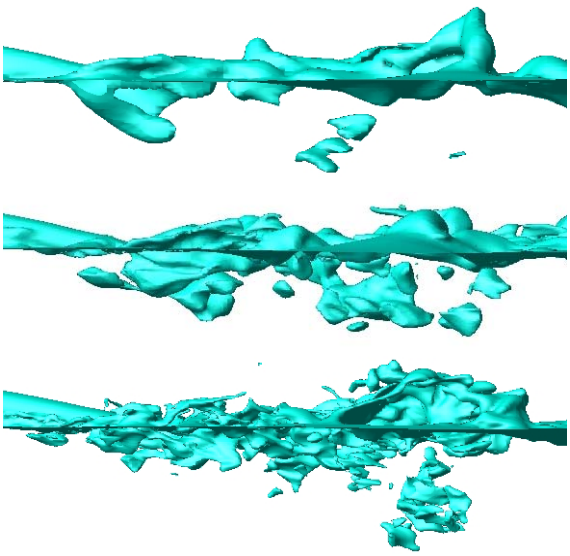

Figure 28: Comparison of the free surface structure for the coarse grid (top), medium (middle) and fine grid (bottom) at 4.2sec, after the plunging jet has fully developed.

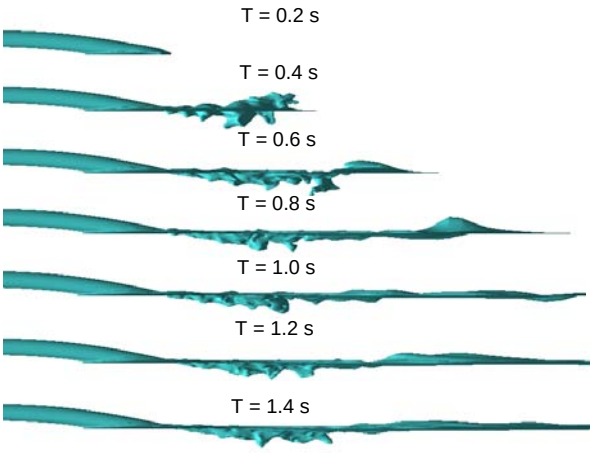

Figure 29: Time sequence of liquid/gas interface deformations for the moving plunging jet. Jet speed=4m/s, translation velocity=2m/s.

In addition to the simulation of stationary plunging jet, we also simulated a moving plunging jet condition as in the experimental study. In the numerical computation a uniform velocity of 2m/s was specified for the pool of water, while the jet velocity at the nozzle exit was kept as 4 m/s. This resulted in a 2m/s relative velocity as the jet impacted on the free surface. Figure 29 shows the evolution of the liquid/air interface over a period of 1.4 seconds. It can be seen that the moving jet wake exhibits significantly different flow characterization when compared with the stationary jet wake. A longer and more structured air pocket under water is observed for the moving plunging jet case. As shown in Figure 30 the number of vortices in the moving jet wake case is much higher and shallower compared to the relatively larger and deeper vortices in the stationary jet wake case. Figure 30 also shows that the numerical results capture qualitatively well the large vortical air pockets. These observations are similar to the experimental observations.

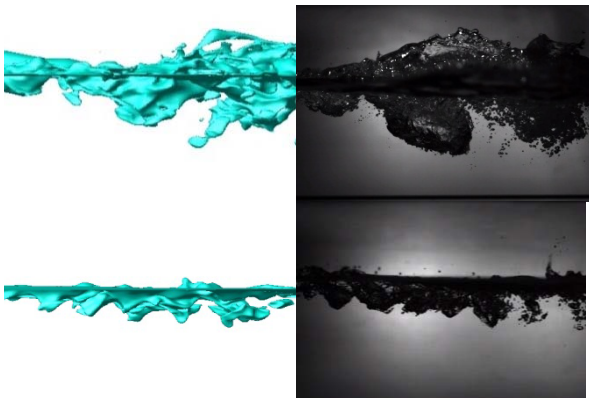

Figure 30: Comparison of the flow structure for stationary jet wake (top) and moving jet wake (bottom), in both the numerical simulations (left) and experimental observations (right).

Validation against Experimental Measurements

To better quantitatively compare the numerical results with the experimental measurements, we also characterized the vortical flow structures from the numerical unsteady solutions using the same image analysis scheme as described in the experimental section. A sequence of images from the numerical solutions for both the moving and stationary jet wakes were analyzed and the frequencies of the appearance of these vortex structures were obtained and compared to the experimental results as shown in Figure 31. It is seen that experiments and simulations give very similar results with the frequency in the case of the moving jet being around one order larger than for the stationary jet case. In general, the frequency gradually reduces as the flow travels downstream. The simulation results are much closer to the experiments near the plunging locations and further downstream,

but deviate a little in the region of air pocket breakup where the image analysis scheme is subject to high uncertainty.

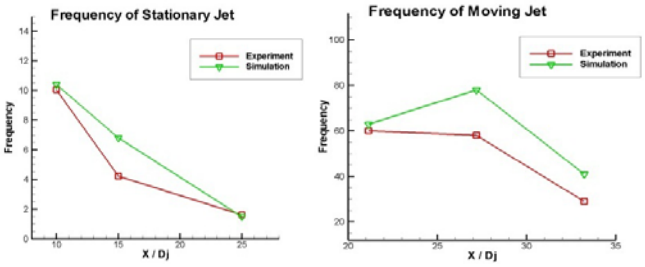

Figure 31: Frequency of the flow structure passage at different downstream locations for both stationary (left) and moving (right) jet wakes.

In order to compare the velocity field between numerical and experimental results we computed time-averaged solutions from the unsteady solutions. After excluding the initial transient period (about 2 seconds), the time-averaged solution was deduced by averaging the time-varying solutions continuously until the averaged result did not vary by more than 1%. The time-averaged solution also excluded the solution on the grid where the gas phase is present. Figure 32 displays the time-averaged streamwise and vertical velocities in the center plane at three streamwise locations.

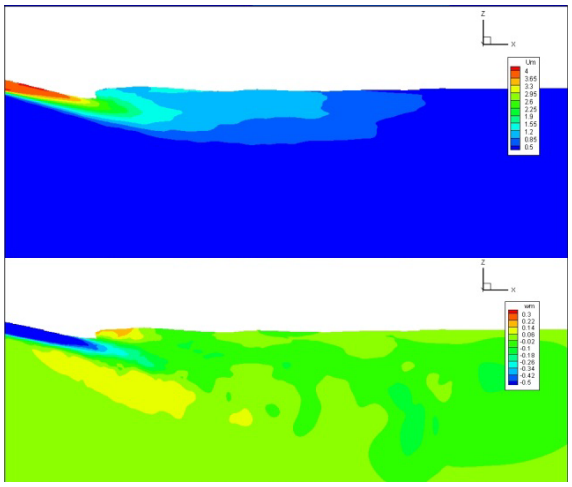

Figure 32: Time-averaged streamwise velocity contours (top) and vertical velocity contours (bottom) in the center plane.

Figure 33 shows a comparison of the time-averaged streamwise velocity profiles at different downstream locations between the three different meshes results and the experimental measurements. It is seen that the streamwise velocity profile is well captured near the plunging region (x = 57.5 cm) except near the maximum velocity region where the Pitot tube measurements are subject to higher uncertainty due to intermittent presence of the gas phase. However, the numerical solution over-predicted the velocity profile at the other two downstream locations. Also, we observe that the difference between the three meshes is quite small. This indicates that the mean flow field is more dependent on the large scale structure of air pockets rather than the small bubbles, and that is why the coarse mesh case was able to predict the velocity profile satisfactorily well since it has successfully captured the former as seen in Figure 28.

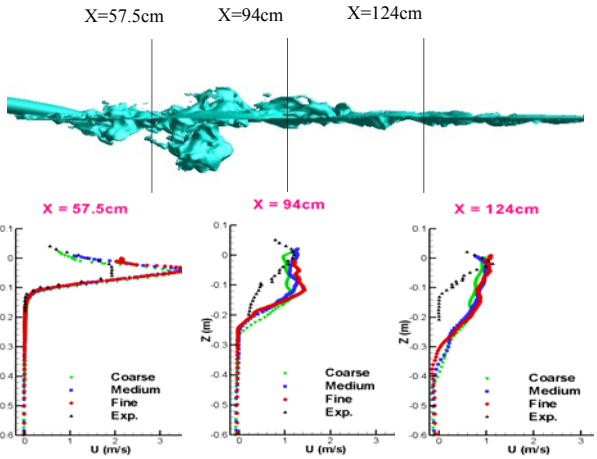

Figure 33: Comparison of time-averaged streamwise velocity profiles between different meshes and the experimental observations at different downstream locations.

Bubble Entrainment due to Plunging Jet

The unsteady solutions of the stationary plunging jet flow obtained from the Eulerian two-phase flow model was used to provide the background flow field for the bubble entrainment model to release the bubbles into the liquid and for the Lagrangian discrete bubble model to track them. Figure 34 shows a time sequence of resulting bubble locations and sizes in the jet wake. For this simulation, we started releasing bubbles when the unsteady computation of the waterjet wake reached T_0 =2 sec.

Figure 35 displays typical pictures of fully developed bubbly jet wake from both experiments and simulations. Generally speaking, the flow regime can be divided into three sub-zones:

a) **Jet impact zone**: the main air volume beneath the still water level is composed of large structures of air pockets generated by the jet impacting the free surface;

b) **Pocket breakup zone**: the air pockets generated in a) are broken into smaller ones and then into small bubbles due to shear effects, thus the total volume of dispersed small bubbles in this zone becomes comparable to that of continuous air pockets;
c) **Diffusion zone**: The pockets or big bubbles have almost totally disappeared due to buoyancy and the above breakup process. The remaining air below the free surface exists in the form of microbubbles which last for a very long time and can be entrained deep in the water.

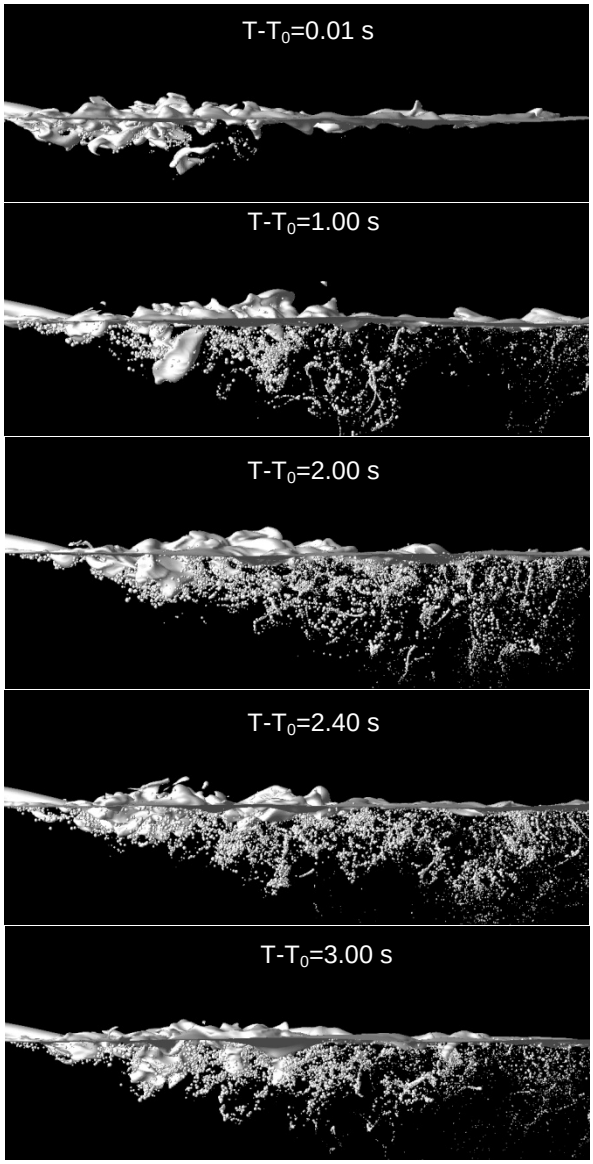

Figure 34: Time sequence of entrained bubble locations and sizes in the jet wake.

By visually comparing the bubble propagation in the numerical simulations with the experimental observations, we can see that while the overall bubble spreading area near the plunging region are similar, the bubbles are carried deeper into the water downstream in the numerical simulations. This implies that the flow field obtained from the Eulerian two-phase flow model has over-predicted the downward velocity. This is probably due to the lack of two-way coupling presently between the two phases. The entrained air pockets are observed to disappear quickly once they break up into small bubbles in the current simulations. This is because the current Level Set scheme does not conserve the air mass and this leads to loss of buoyancy which reduces the downward velocity following the jet impact.

To improve the simulations we will in the future either couple the current Level Set model with a VOF method to conserve mass or simulate better the bubble entrainment with an Eulerian/Lagrangian two-way coupled model.

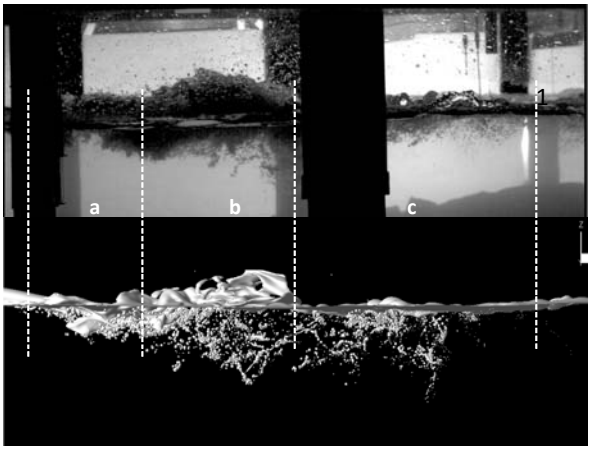

Figure 35: Fully established bubbly wake flow pattern Experiment (top) and 3DYNAFS simulations (bottom).

CONCLUSIONS

We have presented in this paper both experimental and numerical studies of the bubble entrainment due to horizontal plunging jets.

The experiments were conducted in DYNAFLOW tanks. A combined PTV and Pitot tube technique was developed to enable the velocity field measurement near the plunging zone.

High speed videos were used to visualize and analyze the flow structure. From the high speed videos it can be seen that a large amount of air is entrained to form a large air pocket region with high vorticity as the jet plunges onto the free surface. The vortical air pocket is generated periodically from the plunging jet and breaks up into larger blobs as it moves

downstream. The large blobs then continue breaking into a bubble clouds as they move downstream and are exposed to the shear. The frequency of vortical air pocket generation was found to depend on the jet conditions and can be normalized with jet parameters, i.e. jet and free surface relative velocity, diameter, and standoff.

In the numerical study, an Eulerian/Lagrangian one-way coupled two-phase flow model incorporated with a Level-Set method and an improved sub-grid bubble entrainment model was developed to predict the bubble entrainment due to the horizontal plunging jet. The numerical results were shown to capture well the flow structures for both stationary and moving plunging jets using a fine grid.

The numerical simulations were also shown to predict well the velocity field near the jet plunging area but seemed to over predict the streamwise velocity profile downstream. By comparing the bubble spreading area with experimental observations, the bubbles were found to be carried deeper into the water downstream the plunging area in the numerical simulations. Lack of buoyancy force due to the presence of the bubbles is suggested as causing such over-prediction because it was not modeled in the current Eulerian/Lagrangian one-way coupled approach.

ACKNOWLEDGMNETS

This work was conducted at DYNAFLOW, INC. (*www.dynaflow-inc.com*) and was supported by the ONR/NUWC STTR Phase I and II monitored by Dr. William Keith. We acknowledge thankfully his support.

REFERENCES

Bin, A., "Gas Entrainment by Plunging Liquid Jets". Chemical Engineering Science, Vol. 48, No. 10, 1993, pp. 3585-3630.

Bosio, J., and Nalnes, D., "Water Velocity Measurements in Air/Water Mixture," Euromech Collogium No. 7, Greenoble, France, 1969.

Chanson, H.,. Air Bubble Entrainment in Free-Surface Turbulent Shear Flows, Academic Press, 1996.

Choi, J.-K., Hsiao, C.-T., and Chahine, G.L., "Tip Vortex Cavitation Inception Study Using the Surface Averaged Pressure (SAP) Model Combined with a Bubble Splitting Model", 25th Symposium on Naval Hydrodynamics, St. John's, NL, Canada, 2004.

Chorin, A.J., "A Numerical Method for Solving Incompressible Viscous Flow Problems," Journal of Computational Physics, Vol. 2, 1967, pp. 12-26.

Dabiri, S., Sirignano, W.A. and Joseph, D.D., "Cavitation in an orifice flow," Physics of Fluids, Vol. 19, 2007.

Deshpande, S.S., Trujillo, M.F., Wu, X., Chahine, G.L. "Computational and Experimental Characterization of a Liquid Jet Plunging into a Quiescent Pool at Shallow Inclination", Int. J. Heat Fluid Flow, in press, 2012.

Dong, R.R., Katz, J., and Huang, T.T., "On the Structure of Bow Waves on a Ship Model", J. Fluid Mechanics, Vol. 346, 1997, pp. 77-115.

Drew, D.A., and Passman, S.L., Theory of Multicomponent Fluids, Vol. 135 of App. Math. Sci. Springer Verlag, 1998.

Duncan, J.H., "Spilling Breakers", Annual Review of Fluid Mechanics, Vol. 33, 2001, pp. 519-547.

Ervine, D., McKeogh, E., and Elsawy, E.,. "Effect of Turbulence Intensity on The Rate of Air Entrainment by Plunging Water Jets". In Institution of Civil Engineers (Part 2), Vol. 69, 1980, pp. 425-445.

Fedkiw, R.P., Aslam, T., Merriman B., and Osher, S.J., "A non-Oscillatory Eulerian Approach to Interface in Multimaterial Flows (the Ghost Fluid Method), J. Comput. Phys. Vol. 154, 1999, pp. 393-427.

Haberman, W.L., and Morton, R.K., "An Experimental Investigation of the Drag and Shape of Air Bubble Rising in Various Liquids," DTMB Report 802, 1953.

Hirt, C.W., and Nichols, B.D., "Volume of Fluid (VOF) Method for Dynamics of Free Boundaries," J. Comp. Phys., Vol. 30, pp. 201-221, 1981.

Hsiao, C.-T., Chahine, G.L., and Liu, H.-L., "Scaling Effects on Prediction of Cavitation Inception in a Line Vortex Flow", Journal of Fluid Engineering, Vol. 125, 2003, pp.53-60.

Hsiao, C.-T., and Chahine, G.L., "Prediction of Vortex Cavitation Inception Using Coupled Spherical and Non-Spherical Models and Navier-Stokes Computations", Journal of Marine Science and Technology, Vol. 8, No. 3, 2003, pp.99-108.

Hsiao, C.-T. and Chahine, G.L., "Scaling of Tip Vortex Cavitation Inception Noise with a Statistic Bubble Dynamics Model Accounting for Nuclei Size Distribution", Journal of Fluid Engineering, Vol. 127, 2005, pp. 55-65.

Hsiao, C.-T., Jain, A., and Chahine, G.L., "Effects of Gas Diffusion on Bubble Entrainment and Dynamics around a Propeller," 26th Symp. on Naval Hydrodynamics, Rome, Italy, 2006.

Kang, M., Fedkiw and Liu, L.D., "A Boundary Condition Capturing Method for Multiphase Incompressible Flow", J. Sci. Comp., Vol. 15, 2000, pp. 323-360.

Kenneth, T.K. and Duncan, J.H., "Air Entrainment Mechanisms in Plunging Jets and Breaking Waves," Ann. Rev. of Fluid Mechanics, Vol. 44, 2012, pp. 563-596.

Kunz, R.F. Boger, D.A., Stinebring, D.R., Chyczewski, T.S., Lindau, J.W. and Gibeling, H.J., "A Preconditioned Navier-Stokes Method for Two-Phase Flows with Application to Cavitation" Computers & Fluids, Vol. 29, 2000, pp. 849-875.

Lafaurie, B., Nardone, C., Scardovelli, R., Zaleski, S., and Zanetti, G., "Modelling Merging and Fragmentation in Multiphase Flows with Surfer," J. Comp. Phys. Vol. 113, 1994, pp. 134-147.

Lahey, Jr. R.T., "On the Computation of Multiphase Flow," J. Nuclear Technology, Vol. 167, 2009, pp. 1-17.

Ma, J., Oberai, A.A., Drew, D.A., Lahey Jr, R.T., and Moraga, F.J., "A Quantitative Sub-Grid Air Entrainment Model for Bubbly Flows-Plunging Jets". Computers & Fluids, Vol. 39, No. 1, 2010, pp. 77–86,.

Ma, J., Oberai, A., Drew, D., Lahey Jr, R.T., and Hyman, M., "A Comprehensive Sub-Grid Air Entrainment Model for RANS Modeling of Free-Surface Bubbly Fows". Journal of Computational Multiphase Flow, Vol. 3, 2011, pp. 41-56.

Martinez-Bazan, C., Montanes, J.L., and Lasheras, J.C., "On the Breakup of an Air Bubble Injection into Fully Developed Turbulent Fow. Part 1. Breakup Frequency", J. Fluid Mech., Vol. 401, 1999, pp.157-182.

Martinez-Bazan, C., Montanes, J.L., and Lasheras, J.C., "On the Breakup of an Air Bubble Injection into Fully Developed Turbulent Fow. Part 2. Size PDF of the resulting daughter bubbles", J. Fluid Mech. , Vol. 401, 1999, pp.183-207.

McKeogh, E.J., and Ervine, D.A.,. "Air Entrainment Rate and Diffusion Pattern of Plunging Liquid Jets". Chemical Engineering Science, Vol. 36, No. 7, 1981, pp. 1161-1172.

Melville, W.K., Loewen, M.R., and Lamarre, E., "Bubbles, Noise and Breaking Waves: A Review of Laboratory Experiments", Natural Physical Sources of Underwater Sound: Sea Surface Sound (2), Kerman, B.R., ed., Kluwer, Dordrecht, 1993, pp. 483-501

Moraga, F.J., Carrica, P.M., Drew, D.A., and Lahey, Jr., R.T., "A Sub-Grid Air Entrainment Model for breaking Bow Waves and Naval Surface Ships". Computers & Fluids, Vol. 37, No. 3, 2008, pp. 281-298.

Muscari, R.D., Mascio, A., "Numerical Modeling of Breaking Waves Generated by a Ship's Hull", Journal of Marine Science and Technology, Vol. 9, No. 4, 2004, pp. 158-170.

Roe, P.L., "Approximate Riemann Solvers, Parameter Vectors, and Difference Schemes," Journal of Computational Physics, Vol. 43, 1981, pp. 357-372

van Leer, B., and Woodward, P.R., "The MUSCL Code for Compressible Flow: Philosophy and Results", B van Leer, PR Woodward - Proc. of the TICOM Conf., Austin, TX, 1979.

Vanden, K.J., and Whitfield, D.L., "Direct and Iterative Algorithms for the Three-Dimensional Euler Equations", AIAA Journal, Vol. 33, No. 5, 1995, pp. 851-858.

Saffman, P.G., "The Lift on a Small Sphere in a Slow Shear Flow", Journal of Fluid Mechanics, Vol..22, 1965, pp.385-400.

Sene, K.J., "Air Entrainment by Plunging Jets". Chemical Engineering Science, Vol. 43, No. 10, 1988, pp. 2615-2623.

Sussman, M., Smereka, P., and Osher, S.,"A Level-Set Approach for Computing Solutions to Incompressible Two-Phase Flow," J. Comp., Phys., Vol. 114, 1994, pp. 146-159.

Sussman, M., Smereka, P., and Osher, S., "An Improved Level Set Approach for Incompressible Two-Phase Flows," J. Comp., Phys., Vol. 148, 1998, pp. 81-124.